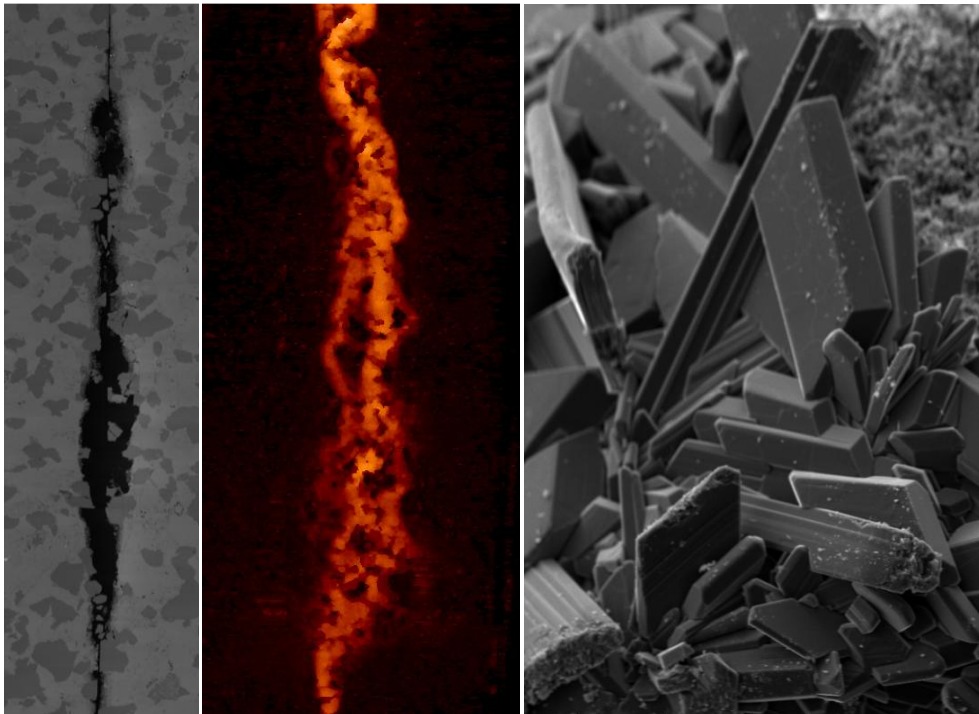


DISSOLVED CO₂ EFFECT
ON THE REACTIVITY OF THE HONTOMÍN
RESERVOIR ROCKS
(LIMESTONE AND SANDSTONE)

María García Ríos



PhD Thesis

Department of Geotechnical Engineering and Geo-Sciences (ETCG)
Technical University of Catalonia (UPC)

Supervisors:

Dr. Jordi Cama

Dra. Linda Luquot

Dr. Josep M. Soler

Institute of Environmental Assessment and Water Research
(IDAEA-CSIC)



CONSEJO SUPERIOR
DE INVESTIGACIONES
CIENTÍFICAS





Acta de calificación de tesis doctoral

Curso académico:

Nombre y apellidos: MARIA OLIMPIA GARCIA RIOS

Programa de doctorado:

Unidad estructural responsable del programa

Resolución del Tribunal

Reunido el Tribunal designado a tal efecto, el doctorando / la doctoranda expone el tema de la su tesis doctoral titulada _____.

Acabada la lectura y después de dar respuesta a las cuestiones formuladas por los miembros titulares del tribunal, éste otorga la calificación:

NO APTO

APROBADO

NOTABLE

SOBRESALIENTE

(Nombre, apellidos y firma)		(Nombre, apellidos y firma)	
Presidente/a		Secretario/a	
(Nombre, apellidos y firma)	(Nombre, apellidos y firma)	(Nombre, apellidos y firma)	(Nombre, apellidos y firma)
Vocal	Vocal	Vocal	Vocal

_____, _____ de _____ de _____

El resultado del escrutinio de los votos emitidos por los miembros titulares del tribunal, efectuado por la Escuela de Doctorado, a instancia de la Comisión de Doctorado de la UPC, otorga la MENCIÓN CUM LAUDE:

SÍ

NO

(Nombre, apellidos y firma)		(Nombre, apellidos y firma)	
Presidente de la Comisión Permanente de la Escuela de Doctorado		Secretario de la Comisión Permanente de la Escuela de Doctorado	

Barcelona a _____ de _____ de _____

TECHNICAL UNIVERSITY OF CATALONIA (UPC)
DEPARTMENT OF GEOTECHNICAL ENGINEERING AND GEO-SCIENCES (ETCG)

Dissolved CO₂ effect on the reactivity of the Hontomín reservoir rocks (limestone and sandstone)

Thesis presented by

María García Ríos

Work conducted in the Institute of Environmental Assessment and Water Research
(IDAEA-CSIC) under the supervision of

Dr. Jordi Cama i Robert

Institute of Environmental Assessment and
Water Research (IDAEA), CSIC

Dra. Linda Luquot

Institute of Environmental Assessment and
Water Research (IDAEA), CSIC

Dr. Josep M. Soler

Institute of Environmental Assessment and
Water Research (IDAEA), CSIC

Barcelona, February 2015



CONSEJO SUPERIOR
DE INVESTIGACIONES
CIENTÍFICAS



This thesis has been funded by CIUDEN (project ALM11/009), Spanish Government Project CGL2010-20984-CO2-01 and the PANACEA project (European Community's Seventh Framework Programme FP7/2007-2013 under grant agreement number 282900).

to The Rivers

Abstract

A test site for CO₂ geological storage is situated in Hontomín (Burgos, northern Spain) with a reservoir rock that is mainly composed of limestone (80-85%) and sandstone (15-20%). The reservoir rock is a deep saline aquifer that is covered by a very low permeability formation which acts as a cap rock. During and after CO₂ injection, since the resident groundwater contains sulfate, the resulting CO₂-rich acid solution gives rise to the dissolution of carbonate minerals (calcite and dolomite) and secondary sulfate-rich mineral precipitation (gypsum or anhydrite) may occur. These reactions that may imply changes in the porosity, permeability and pore structure of the repository could vary the CO₂ storage capacity and injectivity of the reservoir rock.

Therefore, **better knowledge about the overall process of gypsum precipitation at the expense of carbonate mineral dissolution in CO₂-rich solutions and its implications for the hydrodynamic properties of the reservoir rocks** is necessary. A first aim of this thesis is to better understand these coupled reactions by assessing the effect that P , $p\text{CO}_2$, T , mineralogy, acidity and solution saturation state exert on these reactions. To this end, experiments using columns filled with crushed limestone or dolostone are conducted under different P - $p\text{CO}_2$ conditions (atmospheric: 1–10^{-3.5} bar; subcritical: 10–10 bar; and supercritical: 150–34 bar), T (25, 40 and 60 °C) and input solution compositions (gypsum-undersaturated and gypsum-equilibrated solutions). The CrunchFlow and PhreeqC (v.3) numerical codes are used to perform 1D reactive transport simulations of the experiments to evaluate mineral reaction rates in the system and quantify the porosity variation along the column.

Within the range of P - $p\text{CO}_2$ and T of this study only gypsum precipitation takes place and this only occurs when the injected solution is equilibrated with gypsum. Under the P - $p\text{CO}_2$ - T conditions, the volume of precipitated gypsum is smaller than the volume of dissolved carbonate minerals, yielding always an increase in porosity ($\Delta\phi$ up to $\approx 4\%$).

A decrease in T favors limestone dissolution regardless of $p\text{CO}_2$ owing to increasing undersaturation with decreasing temperature. However, gypsum precipitation is favored at high T and under atmospheric $p\text{CO}_2$ conditions but not at high T and under 10 bar of $p\text{CO}_2$

conditions. The increase in limestone dissolution with $p\text{CO}_2$ is directly attributed to pH, which is more acidic at higher $p\text{CO}_2$.

Limestone dissolution induces late gypsum precipitation (long induction time) in contrast to dolostone dissolution, which promotes rapid gypsum precipitation. Moreover, owing to the slow kinetics of dolomite dissolution with respect to that of calcite, both the volume of dissolved mineral and the increase in porosity are larger in the limestone experiments than in the dolostone ones under all $p\text{CO}_2$ conditions ($10^{-3.5}$ and 10 bar).

By increasing $p\text{CO}_2$, carbonate dissolution occurs along the column whereas it is localized in the very inlet under atmospheric conditions. This is due to the buffer capacity of the carbonic acid, which maintains pH at around 5 and keeps the solution undersaturated with respect to calcite and dolomite along the column.

1D reactive transport simulations reproduce the experimental data (carbonate dissolution and gypsum precipitation for different P - $p\text{CO}_2$ - T conditions). Drawing on reaction rate laws in the literature, the reactive surface area to fit the models to the experimental data is used. The values of the reactive surface area are much smaller than those calculated from the geometric areas, given by the transport control of the dissolution reactions.

Given that Hontomín reservoir rock is a fractured system, understanding reaction-induced changes in fracture hydrodynamic properties as a result of contact with acidic fluids is essential for predicting subsurface flows, such as leakage, injectability, and fluid production. Considering this, the second aim of this thesis is to **characterize the overall evolution of a fracture in contact with CO_2 -rich solutions under different flow rates**. Also, the geochemical response of two fractured Hontomín reservoir rocks (limestone and sandstone) to injection of a CO_2 -rich solution is compared. Hence, a set of percolation experiments which consist of injecting CO_2 -rich solutions through fractured limestone and sandstone cores are performed under $P = 150$ bar and $T = 60$ °C at different flow rates ranging from 0.2 to 60 mL/h and sulfate-rich and sulfate-free solutions.

Variation in fracture volume induced by calcite dissolution and gypsum precipitation is measured by means of X-ray computed microtomography (XCMT) and aqueous chemistry. The influence of the flow rate on fracture evolution is accurately evaluated. By increasing the flow rate, under the same pH and far from equilibrium conditions, the volume of dissolved calcite per time increases, confirming that calcite dissolution in the fracture is transport

controlled. In addition, the formation of more uniform geometries under fast flow rates seems to favor calcite dissolution.

The formed dissolution patterns vary from face dissolution to wormhole formation and uniform dissolution by increasing the flow rate (*i.e.*, Pe from 1 to 346). Variation in fracture permeability is also measured and is found to be highly dependent on the flow rate and developed dissolution pattern. Fracture permeability always increases regardless the sulfur content of the injected solution.

On the basis of the obtained experimental results, limestone and sandstone reservoir rocks can be evaluated to identify the most favorable geological context within the reservoir for injection and storage of CO_2 . In addition, 2D reactive transport models that reproduce the variation in aqueous chemistry and fracture geometry of the experiments are performed to estimate flow and reaction kinetics parameters.

Resum

Una planta pilot per a l'emmagatzematge geològic de CO₂ es troba a Hontomín (Burgos). El reservori és un aquífer salí profund, format principalment per roca calcària (80-85%) i gres (15-20%), que està situat entre dues capes de molt baixa permeabilitat que actuen com a roques segell. La dissolució de CO₂ a l'aigua del reservori provocarà una disminució del pH i, en conseqüència, la dissolució dels carbonats presents en el reservori. Tenint en compte que l'aigua resident és rica en sulfat, és possible la precipitació de minerals secundaris (guix o anhidrita). Aquestes reaccions poden provocar canvis en la porositat, la permeabilitat i l'estructura de por del reservori que, a la vegada, poden afectar la seva injectivitat i capacitat d'emmagatzematge.

Per tant, cal aprofundir en el **coneixement sobre els processos acoblats de precipitació de guix i dissolució de carbonats (calcita i dolomita) en solucions riques en CO₂ dissolt i les seves implicacions en les propietats hidrodinàmiques de la roca reservori**. Un primer objectiu d'aquesta tesi és poder comprendre millor aquestes reaccions acoblades mitjançant l'avaluació de l'efecte que exerceixen la pressió P , la pressió parcial de CO₂ $p\text{CO}_2$, la temperatura T , la mineralogia, l'acidesa i l'estat de saturació de la solució sobre aquestes reaccions. Amb aquest objectiu, s'han realitzat una sèrie d'experiments utilitzant columnes plenes de roca calcària o dolomia triturada sota diferents condicions de P - $p\text{CO}_2$ (atmosfèrica: 1-10-3.5 bar; subcrítica: 10-10 bar, i supercrítica: 150-34 bar), T (25, 40 i 60 °C) i composició de la solució d'entrada (solucions subsaturades o equilibrades amb guix). Els codis numèrics CrunchFlow i PhreeqC (v.3) s'han utilitzat per realitzar simulacions de transport reactiu dels experiments en columna amb l'objectiu d'avaluar les velocitats de reacció en el sistema i quantificar la variació de la porositat al llarg de la columna.

En les condicions de P - $p\text{CO}_2$ - T estudiades, la precipitació de guix únicament té lloc quan la solució injectada està en equilibri amb guix. A més, el volum de guix precipitat és menor que el volum de carbonat dissolt, originant sempre un augment de porositat ($\Delta\phi$ fins $\approx 4\%$).

Una disminució en la T afavoreix la dissolució de la calcària independentment de la $p\text{CO}_2$ degut a l'augment de la subsaturació. No obstant, la precipitació de guix està afavorida a alta T per condicions atmosfèriques, originant-se l'efecte contrari per condicions subcrítiques.

L'augment de la $p\text{CO}_2$ comporta un augment en la dissolució de calcària, fet que és directament atribuït a l'efecte del pH, que és més àcid a major $p\text{CO}_2$.

La dissolució de calcària comporta un retard en la precipitació de guix (llarg temps d'inducció), al contrari del que passa amb la dissolució de dolomia que promou una ràpida precipitació de guix. A més, a causa de la lenta cinètica de dissolució de la dolomita amb respecte a la de la calcita, el volum de mineral dissolt i l'augment de porositat són majors en els experiments amb calcària sota totes les condicions de $p\text{CO}_2$ estudiades.

La dissolució del carbonat es produeix al llarg de tota la columna quan la $p\text{CO}_2$ és alta (10 and 34 bar) i, en canvi, es localitza a l'entrada de la columna sota condicions atmosfèriques. Aquesta diferència és deguda a la capacitat tampó de l'àcid carbònic, ja que manté el pH al voltant de 5 i la solució subsaturada pel que fa a la calcita i a la dolomita al llarg de la columna.

Les simulacions de transport reactiu (1D) reproduïxen les dades experimentals (dissolució de carbonat i precipitació de guix per a les diferents condicions de P - $p\text{CO}_2$ - T). En base a les lleis de velocitat de reacció que es troben en la literatura, s'han fet servir els valors de les àrees reactives per realitzar l'ajust del model a les dades experimentals. Aquests valors són bastant inferiors als inicialment calculats a partir de les àrees geomètriques, ja que les reaccions de dissolució estan controlades pel transport.

La roca reservori a Hontomín està significativament fracturada. Per tant, entendre els canvis en les propietats hidrodinàmiques de les fractures, induïts per reaccions de dissolució/precipitació, és essencial per predir els possibles fluxos subterranis tals com fuites, injectivitat o producció de fluids. Tenint en compte això, el segon objectiu d'aquesta tesi és **caracteritzar l'evolució de fractures en contacte amb solucions riques en CO_2 a diferents cabals**. També es compara la resposta geoquímica a la injecció de CO_2 de les dues roques principals del reservori (calcària i gres). Així doncs, es realitza un conjunt d'experiments de percolació que consisteixen en injectar solucions riques en CO_2 (sense sulfat i riques en sulfat) a través de roques de calcària i gres fracturades, sota $P = 150$ bar i $T = 60$ °C i a diferents cabals compresos entre 0,2 i 60 ml/h. La variació del volum de fractura, induïda per la dissolució de calcita i la precipitació de guix, es mesura mitjançant microtomografia de raigs X (XCMT) i la química de la solució. S'avalua també la influència del cabal en l'evolució de la fractura i s'obté que el volum de calcita dissolta per unitat de temps augmenta augmentant el cabal, la qual cosa confirma que la dissolució en la fractura està controlada pel

transport. També s'observa que la formació de geometries més uniformes a cabals més ràpids pot afavorir la dissolució de la calcita.

Els patrons de dissolució varien de 'face dissolution' a 'wormhole' i a 'uniform dissolution' a mesura que s'augmenta el cabal (és a dir, número de Péclet Pe d'1 a 346). S'observa que la variació de permeabilitat de la fractura depèn del cabal i del patró de dissolució desenvolupat. La permeabilitat de la fractura sempre augmenta, independentment del contingut de sulfat de la solució d'entrada.

En base als resultats experimentals obtinguts amb les roques d'Hontomín, s'avalua quin seria el context geològic més favorable en el reservori per a la injecció i emmagatzematge del CO_2 . A més a més, es realitzen models de transport reactiu (2D) dels experiments de percolació amb fractures per estimar els paràmetres cinètics i de flux.

Resumen

Una planta piloto para el almacenamiento geológico de CO₂ se ubica en Hontomín (Burgos). El reservorio es un acuífero salino profundo que se compone principalmente de roca caliza (80-85%) y arenisca (15-20%). Éste está situado entre dos capas de muy baja permeabilidad que actúan como rocas sello. La disolución de CO₂ en el agua presente en el reservorio provocará una disminución del pH y, en consecuencia, la disolución de los carbonatos presentes en el reservorio. Además, como la solución residente es rica en sulfato, es posible la precipitación de minerales secundarios (yeso o anhidrita). Estas reacciones pueden provocar cambios en la porosidad, permeabilidad y estructura de poro del reservorio que, a su vez, pueden hacer variar su inyectabilidad y capacidad de almacenamiento.

Por todo ello, es necesario profundizar en el **conocimiento sobre los procesos acoplados de precipitación de yeso y disolución de carbonatos (calcita y dolomita) en soluciones ricas en CO₂ disuelto y sus implicaciones en las propiedades hidrodinámicas de la roca reservorio**. Un primer objetivo de esta tesis es comprender mejor estas reacciones acopladas mediante la evaluación del efecto que ejercen la presión P , la presión parcial de CO₂ $p\text{CO}_2$, la temperatura T , la mineralogía, la acidez y el estado de saturación de la solución sobre estas reacciones. Con este objetivo, se han realizado una serie de experimentos utilizando columnas llenas de roca caliza o dolomía triturada bajo diferentes condiciones de P - $p\text{CO}_2$ (atmosférica: 1-10^{-3.5} bar; sub-crítica: 10-10 bar, y supercrítica: 150-34 bar), T (25, 40 y 60 ° C) y composición de la solución de entrada (soluciones sub-saturadas o equilibradas con respecto al yeso). Los códigos numéricos CrunchFlow y PhreeqC (v.3) se han utilizado para realizar simulaciones de transporte reactivo de los experimentos en columna con el objetivo de evaluar las velocidades de reacción en el sistema y cuantificar la variación de la porosidad a lo largo de la columna.

En las condiciones de P - $p\text{CO}_2$ - T estudiadas, la precipitación de yeso únicamente tiene lugar cuando la solución inyectada está en equilibrio con yeso. Además, el volumen de yeso precipitado es menor que el volumen de carbonato disuelto, originando siempre un aumento de porosidad ($\Delta\phi$ hasta $\approx 4\%$).

Una disminución en la T favorece la disolución de la caliza independientemente de la $p\text{CO}_2$ debido al aumento de la sub-saturación. Sin embargo, hay un aumento en la precipitación de

yeso a alta T para condiciones atmosféricas, viéndose el efecto contrario para condiciones sub-críticas. El aumento de la $p\text{CO}_2$ conlleva un aumento en la disolución de caliza, hecho que es directamente atribuido al efecto del pH, que es más ácido a mayor $p\text{CO}_2$.

La disolución de caliza conlleva un retraso en la precipitación de yeso (largo tiempo de inducción), lo contrario que ocurre con la disolución de dolomía que promueve una rápida precipitación de yeso. Además, debido a la lenta cinética de disolución de la dolomita con respecto a la de la calcita, el volumen de mineral disuelto y el aumento de porosidad son mayores en los experimentos con caliza bajo todas las condiciones de $p\text{CO}_2$ estudiadas.

La disolución del carbonato se produce a lo largo de toda la columna cuando la $p\text{CO}_2$ es alta (10 and 34 bar) y, en cambio, se localiza en la entrada de la columna bajo condiciones atmosféricas. Esta diferencia es debida a la capacidad tampón del ácido carbónico, ya que mantiene el pH alrededor de 5 y mantiene la solución sub-saturada con respecto a la calcita y a la dolomita a lo largo de la columna.

Las simulaciones de transporte reactivo (1D) reproducen los datos experimentales (disolución de carbonato y precipitación de yeso para las diferentes condiciones de P - $p\text{CO}_2$ - T). En base a las leyes de velocidad de reacción que se encuentran en literatura, se han usado los valores de las áreas reactivas para realizar el ajuste del modelo a los datos experimentales. Estos valores son bastante inferiores a los inicialmente calculados a partir de las áreas geométricas, debido a que las reacciones de disolución están controladas por el transporte.

La roca reservorio en Hontomín está significativamente fracturada. Por lo tanto, entender los cambios en las propiedades hidrodinámicas de las fracturas, inducidos por reacciones de disolución/precipitación, es esencial para predecir los posibles flujos subterráneos como fugas, inyectabilidad o producción de fluidos. Teniendo en cuenta esto, el segundo objetivo de esta tesis es **caracterizar la evolución de fracturas que estén en contacto con soluciones ricas en CO_2 a diferentes caudales**. Además, se compara la respuesta geoquímica a la inyección de CO_2 de las dos rocas principales del reservorio (caliza y arenisca). Para ello, se realiza un conjunto de experimentos de percolación que consisten en inyectar soluciones ricas en CO_2 (sin sulfato y ricas en sulfato) a través de rocas de caliza y arenisca fracturadas. Todos ellos bajo $P = 150$ bar y $T = 60$ °C y a diferentes caudales comprendidos entre 0,2 y 60 mL/h. La variación del volumen de fractura, inducida por la disolución de calcita y la precipitación de yeso, se mide mediante micro-tomografía de rayos X (XCMT) y la química de la solución. Se evalúa también la influencia del caudal en la

evolución de la fractura, obteniéndose que aumentando el caudal el volumen de calcita disuelta por unidad de tiempo aumenta, confirmando así que la disolución en la fractura está controlada por el transporte. También se observa que la formación de geometrías más uniformes a caudales más rápidos puede favorecer la disolución de calcita.

Los patrones de disolución varían de ‘face dissolution’ a ‘wormhole’ y a ‘uniform dissolution’ a medida que aumenta el caudal (es decir, números de Péclet Pe de 1 a 346). Se mide también la variación de permeabilidad de la fractura encontrando que su evolución depende del caudal y del patrón de disolución desarrollado. La permeabilidad de la fractura siempre aumenta independientemente del contenido de sulfato de la solución de entrada.

En base a los resultados experimentales obtenidos con las rocas de Hontomín, se evalúa cuál sería el contexto geológico más favorable en el reservorio para la inyección y almacenamiento del CO_2 . Además, se realizan modelos de transporte reactivo (2D) de los experimentos de percolación con fracturas para estimar los parámetros cinéticos y de flujo.

Agraïments

Quin moment!...això és el que diria un gran amic meu!

Ja ha arribat! i he de reconèixer que el camí no ha estat fàcil. Un camí on hi ha tants forats que agraeixes sincerament que algú et doni un cop de mà. I per això estic aquí, per agrair a tots aquells que en el algun moment s'han parat al costat meu, han vist que necessitava ajuda i me l'han ofert. Ajuda de tota mena, és clar!

...durant les hores llargues del dia, quan estem treballant: gràcies al **Víctor**, al **Francesco**, a la **Cris**, a la **Gaby**, a l'**Anna Russian** i a la **Yoar** per fer que aquestes hores passin de manera més lleugera, per distreure'm, fer-me riure i per aguantar-me en aquells moments on sembla que tot és negre. A l'**Ester** per la seva disponibilitat a l'hora d'ajudar-te en qualsevol problema o de passar una estona agradable xerrant. Al **Carles Ayora** i al **Josep Soler** per la seva ajuda incondicional. A la **Linda** per la seva ajuda amb condicions (li dec molta pasta!) però sempre amable i profitosa.

...quan arribes a casa tot cansat: gràcies al **Josevi** per ser tant pacient i agradable amb mi sempre, per treure'm un somriure i per calmar el monstre que tinc a dintre que, a vegades, vol sortir. Abans del Josevi altres m'han patit i/o gaudit. Agrair també a tots aquells que han compartir pis amb mi durant tots aquests anys menjant-se amb patates els dies bons i també els dolents: gràcies a la gent de Sant Eusebi (el **Davik**, el **Kike**, l'**Elisa** i la **Dèlia**) i el meu estimat amic **Lluís**.

...quan és divendres i vols trobar-te amb la teva gent, la de tota la vida o no, on tot val i tot s'entén perquè et fan sentir sempre com a casa (la família!): gràcies al **Rubén**, a la **Laura**, a l'**Anna**, a la **Rosa**, a la **Mònica**, al **Servando** i a la **Marta**. Gràcies també a les meves nenes amb les que no només he compartit això sinó quasi tota una vida: gràcies a la **Patri**, a la **Susana** i a la **Lorena**. Gràcies també a l'**Ana** pels moments tant especials juntes.

...en tots els moments: gràcies a **la meva mare**, **el meu pare** i la meva cosina **Txell** per formar una família acollidora i agradable i per sempre donar-me suport.

I sobretot gràcies al meu director de tesi, el **Jordi Cama**, perquè sense ell tot això no hagués estat possible. Gràcies per totes les vegades que m'has vist fluixa i m'has aixecat i també per aquelles que m'has vist forta i has compartit amb mi el moment. Ha estat un plaer!

Table of contents

PART I: INTRODUCTION and MATERIALS AND METHODS 1

Chapter 1

Introduction..... 3

- 1.1 Background and objectives 3
- 1.2 Thesis outline 11

Chapter 2

Materials and methods 13

- 2.1 Experimental methodology 13
 - 2.1.1 Sample characterization and analytical techniques 13
 - 2.1.2 Injected solutions 17
 - 2.1.3 Experimental setups and conditions 20
 - 2.1.3.1. Atmospheric pressure setup ($P = 1$ bar) 21
 - 2.1.3.2. Subcritical pressure setup ($P = 10$ bar) 21
 - 2.1.3.3. Supercritical pressure setup ($P = 150$ bar) 23
 - 2.1.4 Mass transfer calculations 24
 - 2.1.5 Permeability changes 26
- 2.2 Reactive transport modeling 27
 - 2.2.1. Description of the CrunchFlow reactive transport code 27
 - 2.2.2 One-dimensional model (*Part II: crushed rock*) 29
 - 2.2.2.1. Numerical discretization 29
 - 2.2.2.2 Rock and solution composition 30
 - 2.2.2.3 Flow and transport properties 30
 - 2.2.2.4 Thermodynamic and kinetic data 31
 - 2.2.2.5 Reaction rates 32
 - 2.2.3 Two-dimensional model (*Part III: fractured cores*) 32
 - 2.2.3.1 Numerical discretization 33

2.2.3.2 Rock and solution composition.....	35
2.2.3.3 Flow and transport parameters.....	35
2.2.3.4 Thermodynamic and kinetic data.....	37
2.2.3.5 Reaction rates.....	37
PART II: CRUSHED ROCK.....	39

Chapter 3

Interaction between CO₂-rich sulfate solutions and carbonate rocks: column experiments and 1D modeling..... 41

3.1 Introduction.....	41
3.2 Results.....	42
3.2.1 Experiments under atmospheric conditions ($P = 1$ bar; $p\text{CO}_2 = 10^{-3.5}$ bar).....	44
3.2.1.1 H ₂ SO ₄ solution (<i>s</i>).....	44
3.2.1.2 Acidic gypsum-equilibrated solution (<i>a2.1</i> and <i>a3.5</i>).....	46
3.2.2 Experiments under subcritical conditions ($P = p\text{CO}_2 = 10$ bar).....	47
3.2.2.1 Gypsum-undersaturated solution (<i>gp-u</i>).....	47
3.2.2.2 Gypsum-equilibrated solution (<i>gp-e</i>).....	47
3.2.3 Experiment under supercritical conditions ($P = 150$ bar; $p\text{CO}_2 = 34$ bar).....	49
3.3 Discussion.....	50
3.4 Summary and conclusions.....	56

PART III: FRACTURED CORES..... 59

Chapter 4

Influence of the flow rate on dissolution and precipitation features during percolation experiment with fractured limestone and sandstone cores..... 61

4.1 Introduction.....	61
4.2 Results.....	62
4.2.1 Initial fracture characterization.....	63
4.2.2 Aqueous chemistry.....	65

4.2.3 Permeability	66
4.2.4 Identification of dissolution and precipitation processes	69
4.2.4.1. Limestone samples	70
4.2.4.2. Sandstone samples	75
4.3 Discussion	79
4.3.1 Fracture volume calculated from mass balance and XCMT	79
4.3.2 Influence of flow rate on reaction	82
4.3.3 Dissolution patterns.....	86
4.3.4 Permeability changes during fracture dissolution	90
4.4 Summary and conclusions	92

Chapter 5

Dissolved CO₂ effect on two fractured reservoir rocks: comparison and 2D modeling..... 95

5.1 Introduction.....	95
5.2 The role of silicate minerals on the CO ₂ storage capacity and injectivity	96
5.3 (2D) Reactive transport modeling.....	99
5.3.1 Face dissolution	99
5.3.2 Wormhole	101
5.3.3 Uniform dissolution	104
5.3.4 Flow and reaction kinetics parameters.....	105
5.4 Summary and conclusions	106

PART IV: CONCLUSIONS.....107

Chapter 6

Conclusions.....109

References115

Appendix A

1D and 2D model parameters129

Appendix B

Additional experimental and modeling results from the column experiments.....139

List of figures

- Fig. 1.1** Total annual anthropogenic GHG emissions (GtCO₂eq/yr) by groups of gases 1970-2010: CO₂ from fossil fuel combustion and industrial processes; CO₂ from Forestry and Other Land Use (FOLU); methane (CH₄); nitrous oxide (N₂O); fluorinated gases covered under the Kyoto Protocol (HFC-PFC-SF₆). Average annual growth rate for each decade is highlighted with the brackets (IPCC, 2014).4
- Fig. 1.2** Scheme of The Compostilla Project (left) and stratigraphic column of the Hontomín site (right; GEOMODELS, University of Barcelona).Depth of CO₂ injection in the reservoir is between 1414-1530 m.6
- Fig. 2.1** Rock samples used in the column experiments described in *Part II: crushed rock*. Top: vuggy limestone (core, crushed grains (1-2 mm)/ground grains (250-500 μm) and SEM image); bottom: dolostone (fragments, crushed grains (1-2 mm) and SEM image). 15
- Fig. 2.2** Fracture core dimensions (a) and SEM images (b) of the rock samples used in the percolation experiments with fractured cores shown in *Part III: fractured cores*. Cal = calcite; Qz = quartz and Mc = microcline. 16
- Fig. 2.3** Experimental setups used to work under atmospheric (a), subcritical (b) and supercritical (c) CO₂ conditions.....20
- Fig. 2.4** Scheme showing the geometry and boundary conditions of the flow domain used in the models: (a) rectangular and (b) cylindrical coordinates. Left and right boundaries are no-flow boundaries. Plots on the left show the conceptual model, and plots on the right show the implemented grid.34
- Fig. 3.1** SEM images of the reacted limestone (a) and dolostone (b). Gypsum needles precipitated on the carbonate surfaces.44
- Fig. 3.2** Top row (experiments *L25-atm-s* and *D25-atm-s*): Variation of the experimental (Exp) and simulated (Sim) output concentration of Ca (a) and S (b) with time in limestone (L; in green) and dolostone (D; in blue) column experiments. Black-solid lines indicate input solution. Dashed and dotted lines depict simulated values of limestone and dolostone column

experiments, respectively. Bottom row (experiments *L25-atm-a2.1* and *D25-atm-a2.1*): Variation of the experimental (Exp) and simulated (Sim) increase in Ca (c) and S (d) concentration with time in limestone column experiments at 25 °C (in green) and 60 °C (in red). Solid lines indicate the Ca concentration increase at equilibrium with calcite.45

Fig. 3.3 Top row (experiments *L25-10-gp-e*, *L40-10-gp-e* and *L60-10-gp-e*): Variation of the experimental (Exp) and simulated (Sim) increase in Ca (a) and S (b) concentration with time in limestone column experiments at 25 °C (in green), 40 °C (in orange) and 60 °C (in red). Dashed, dotted and red-solid lines show simulated values at 25, 40 and 60 °C, respectively. Bottom row (experiments *L40-10-gp-e* and *D40-10-gp-e*): Variation of the experimental (Exp) and simulated (Sim) increase in Ca (c) and S (d) concentration versus time in limestone (L; in orange) and dolostone (D; in blue) column experiments. Dotted and dashed lines show simulated values of limestone and dolostone experiments, respectively. Solid lines in (c) represent the Ca concentration increase in equilibrium with calcite (in orange) and dolomite (in blue).48

Fig. 3.4 Variation of the experimental (Exp) and simulated (Sim) output Ca and Mg (a) and S (b) concentration with time in the limestone column experiment under supercritical conditions (*L60-34-gp-e*). Red and green dashed lines indicate simulated values of output concentrations using CrunchFlow and PhreeqC (v.3), respectively. In the PhreeqC (v.3) calculation, dolomite was not considered and the calculated output S concentration coincides with the input value.50

Fig. 3.5 Experimental variation of volume of dissolved rock $V_{rock-diss}$ (a and d), percentage of volume of dissolved limestone (g), volume of precipitated gypsum V_{Gp-ppt} (b and e), percentage of volume of precipitated gypsum (h) and porosity $\Delta\phi$ (c, f and i) with number of pore volumes V_p in experiments performed at 25 °C (in green), 40 °C (in orange) and 60 °C (in red). Solid, dashed and dotted lines (plots of T and pCO_2) represent atmospheric, 10 bar and 34 bar pCO_2 conditions, respectively. Solid lines and solid lines with empty squares (plots of mineralogy) indicate experiments with limestone (L) and dolostone (D), respectively. V_{L-diss} (%) and V_{Gp-ppt} (%) are percentages of dissolved and precipitated volumes with respect to each initial sample volume.51

Fig. 3.6 Modeled porosity variation along the column during experiments at 25 °C (in green), 40 °C (in orange) and 60 °C (in red). Solid, dashed and dotted lines represent atmospheric, 10 bar and 34 bar pCO_2 conditions, respectively, and plain and empty-square lines indicate experiments with limestone and dolostone, respectively. Colored areas indicate simulated values using the initial (A_{Gp-0}) and final (A_{Gp-f}) gypsum reactive area. T effect under atmospheric and 10 bar of pCO_2 , respectively (a and b), mineralogy effect (c) and pCO_2 effect on porosity changes (d). Variation of calcite saturation index (SI_{Cal}) along the column is shown in (a, b and d).52

Fig. 4.1 Variation in the increase of Ca (a) and S (b) concentrations over time in the percolation experiments with fractured limestone cores, using *no-s* input solution (open symbols) and *gp-e* input solution (solid symbols) at $Q = 0.2$ mL/h (in violet), $Q = 1$ mL/h (in green), $Q = 5$ mL/h (in red) and $Q = 60$ mL/h (in black). Time for experiments at $Q = 0.2, 1$ and 5 mL/h is plotted in the lower x -axis and time for experiments at $Q = 60$ mL/h is plotted in the upper x -axis.65

Fig. 4.2 Variation in the increase of Ca (left column-a) and S and Si (right column-b) concentrations over time in the percolation experiments with fractured sandstone cores, using *no-s* input solution (open symbols), *gp-u* solution (semi-solid symbols) and *gp-e* input solution (solid symbols) at $Q = 0.2$ mL/h (in violet), $Q = 1$ mL/h (in green), $Q = 5$ mL/h (in red) and $Q = 60$ mL/h (in black). Dotted lines in (a) indicate Ca concentrations and solid and dashed lines in (b) indicate Si and S concentrations, respectively.67

Fig. 4.3 Variation in fracture permeability during limestone (dashed lines-a) and sandstone (solid lines-b) experiments. $Q = 1$ mL/h (green line), $Q = 5$ mL/h (red and pale red lines) and $Q = 60$ mL/h (black and grey lines). In the plots with grey background, upper- x axis indicates time for exp. *L1-no-s* and *S5-gp-e* and lower- x axis shows time for exp. *L5-gp-e*, *S1-no-s* and *S5-no-s*.68

Fig. 4.4 SEM images and MicroRaman spectrum of a thin section (section 2 in Fig. 2.2a) from the reacted fracture in experiment *L5-gp-e*: (a) dissolved calcite in the fracture surfaces and precipitated gypsum crystals. (b) Detailed view of the gypsum (Gp) crystals that grow at the expense of calcite (Cal) dissolution. Note the strong alteration of the fracture surfaces leading to formation of high microporosity. The y values indicate the distance from the inlet ($y = 0$) of the fracture along the flow direction (y). (c) MicroRaman spectra. The presence of the two characteristic peaks of water at ≈ 3500 cm^{-1} confirms that gypsum is the sulfate precipitated phase. The standard spectra of gypsum and anhydrite are from Downs (2006). .69

Fig. 4.5 SEM images of the reacted limestone fractures in experiments with *no-s* input solution at (a) $Q = 1$ mL/h (*L1-no-s*, section 1) and (b) $Q = 60$ mL/h (*L60-no-s*, section 2). Red-dotted arrows indicate where the initial fracture aperture was measured (Table 4.2). The y values indicate the distances from the inlet ($y = 0$) of the fracture along the flow direction (y). Yellow arrows in (a) point out core heights, which are given by the y values (mm). 71

Fig. 4.6 SEM images of the reacted limestone fractures in experiments with *gp-e* input solution at (a) $Q = 0.2$ mL/h (*L0.2-gp-e*, section 1), (b) $Q = 1$ mL/h (*L1-gp-e*, section 2), (c) $Q = 5$ mL/h (*L5-gp-e*, section 2) and (d) $Q = 60$ mL/h (*L60-gp-e*, section 1). Precipitated gypsum and development of microporosity (rough fracture surface) are observed in

experiments at $Q = 1$ and 5 mL/h. Smooth fracture surface is observed in the experiment at $Q = 60$ mL/h. The y values indicate the distances from the inlet ($y = 0$) of the fracture along the flow direction (y). Yellow arrows in (a) and (d) point out the core height, which is given by the y value (mm). 72

Fig. 4.7 XCMT results. Total volume of reacted (A) and unreacted (A') fractures and images of the precipitated gypsum (B) in limestone experiments with *no-s* solution at (a) $Q = 1$ mL/h and (b) $Q = 60$ mL/h and experiments with *gp-e* solution at (c) $Q = 1$ mL/h, (d) $Q = 5$ mL/h and (e) $Q = 60$ mL/h. Arrows indicate bends of the preferential flow channels. Color scale bars are in pixels (1 pixel = $14 \mu\text{m}$). Black and white sections (perpendicular to flow) show the fracture morphology with associated dissolution patterns from the inlet (right) to the outlet (left) of the cores. 74

Fig. 4.8 Fracture-length profiles that show the volume of unreacted (blue lines) and reacted (black lines) fractures, the largest connected volume from dissolution (orange lines) and the volume of precipitated gypsum (red lines) in exps. with *no-s* solution at (a) $Q = 1$ mL/h and (b) $Q = 60$ mL/h, and exps. with *gp-e* solution at (c) $Q = 1$ mL/h, (d) $Q = 5$ mL/h and (e) $Q = 60$ mL/h. Arrows point out volume increases that took place at the bends of the preferential flow channels (see Fig. 4.7). 75

Fig. 4.9 SEM images of the reacted sandstone fractures in experiments with *no-s* input solution at (a) $Q = 1$ mL/h (*S1-no-s*), (b) $Q = 5$ mL/h (*S5-no-s*) and (c) $Q = 60$ mL/h (*S60-no-s*). The y values indicate the distances from the inlet ($y = 0$) of the fracture along the flow direction (y). Yellow arrows point out the core height, which is given by the y value (mm).. 75

Fig. 4.10 SEM images of the reacted sandstone fractures in experiments with *gp-e* input solution at (a) $Q = 0.2$ mL/h (*S0.2-gp-e*), (b) $Q = 1$ mL/h (*S1-gp-e*), (c) $Q = 5$ mL/h (*S5-gp-e*) and (d) $Q = 60$ mL/h (*S60-gp-e*). Close-up images in (b) show precipitated gypsum (left) and precipitated unidentified aluminosilicate (right). The y values indicate the distances from the inlet ($y = 0$) of the fracture along the flow direction (y). Yellow circle in (d) indicates a possible site of a grain detachment. 77

Fig. 4.11 XCMT results. Total volume of reacted (A) and unreacted (A') fractures in sandstone experiments with *no-s* solution at (b) $Q = 5$ mL/h and (c) $Q = 60$ mL/h, with *gp-u* solution at (d) $Q = 5$ mL/h and (e) $Q = 60$ mL/h and with *gp-e* solution at (f) $Q = 1$ mL/h and (h) $Q = 60$ mL/h. XCMT was not performed in experiment *S1-no-s* and XMT analysis was not carried out in experiment *S5-gp-e*. Color scale bars are in pixels (1 pixel = $14 \mu\text{m}$). Black and white sections (perpendicular to flow) show the fracture morphology with associated dissolution patterns from the inlet (left) to the outlet (right) of the cores. 78

Fig. 4.12 Fracture-length profiles that show the volume of unreacted (blue lines) and reacted (black lines) fractures and the largest connected volume from dissolution (orange lines) in sandstone experiments with *no-s* solution at (b) $Q = 5$ mL/h and (c) $Q = 60$ mL/h, experiments with *gp-u* solution at (d) $Q = 5$ mL/h, (e) $Q = 60$ mL/h and experiments with *gp-e* solution at (f) $Q = 1$ mL/h and (h) $Q = 60$ mL/h. 79

Fig. 4.13 Dissolution patterns, as a function of Péclet and Damköhler numbers, of limestone and sandstone experiments performed in this study and limestone experiments conducted by Elkhoury et al. (2013). The dashed arrow shows the tendency of dissolution patterns by increasing flow rate. The triangle, square and circle symbols indicate face dissolution, wormhole and uniform dissolution, respectively. The mixed (semicircle-square) symbol denotes transition between patterns (see text). 88

Fig. 4.14 Variation in fracture permeability vs. the number of equivalent fracture volumes (time/residence time τ) for the limestone (dashed lines) and sandstone (solid lines) experiments. $Q = 1$ mL/h (green line), $Q = 5$ mL/h (red and pale red lines) and $Q = 60$ mL/h (black and grey lines). $k(t_0)$ indicates initial fracture permeability. 91

Fig 5.1 Experimental variation of volume of dissolved rock $V_{rock-diss}$ (a), volume of precipitated gypsum V_{gp-ppt} (b) and fracture volume ΔV (c) with time in limestone (dashed lines) and sandstone (solid lines) experiments with *gp-e* input solution, under $Q = 0.2$ mL/h (in violet), $Q = 1$ mL/h (in green), $Q = 5$ mL/h (in red) and $Q = 60$ mL/h (in black). 97

Fig. 5.2 Variation in fracture permeability as a function of number of fracture volumes (t/τ) and the associated distribution of created volume in the experiments *L60-gp-e* (a) and *S60-gp-e* (b). $k(t_0)$ indicates initial fracture permeability. 98

Fig. 5.3 Experiment *L0.2-gp-e* (face dissolution); simulations with rectangular coordinates and flow update: (a,b) Variation in the experimental and simulated Ca and S concentration versus time and (c,d) simulated porosity variation with distance normal to fracture. Colored areas in (c,d) indicate the zone with 100 % porosity measured by SEM at the inlet of the fractured core. 100

Fig. 5.4 Velocity field for experiment *L0.2-gp-e* (face dissolution) at $t = 46$ h; Velocity ($m^3/m^2/yr$) in the x direction (V_x ; left plot) and in the y direction (V_y ; right plot). 101

Fig. 5.5 Experiment *L1-gp-e* (wormhole); simulations with rectangular coordinates (rect) and flow update (solid lines) and simulations with cylindrical coordinates (cyl) and fixed flow

(dashed lines): Variation in the experimental and simulated Ca (a) and S (b) concentration versus time. r indicates the initial radius of the cylinder (see text)..... 102

Fig. 5.6 Experiment *L1-gp-e* (wormhole); simulation with rectangular + cylindrical coordinates and fixed flow: (a,b) Variation in the experimental and simulated Ca and S concentration versus time and variation in simulated porosity (c) and mineral content (d) with distance normal to fracture..... 103

Fig. 5.7 Experiment *S60-no-s* (uniform dissolution); simulation with rectangular coordinates and flow update: (a) Variation in the experimental and simulated Ca concentration versus time and (b) simulated porosity variation with the distance normal to fracture. Grey area in (b) indicates the zone with high porosity (96%) measured by SEM along most the fracture length..... 104

Fig. B.1 Variation of experimental (Exp) and simulated (Sim) output pH (a) and output concentration of Ca (b), Mg (c) and S (d) with time in limestone (L; in green) and dolostone (D; in blue) column experiments (*L25-atm-s* and *D25-atm-s*, respectively). Solid lines indicate input solution except for Mg which is smaller than 3×10^{-4} mol/kgw (Table 2.2). Dashed and dotted lines indicate simulated values of limestone and dolostone column experiments, respectively..... 140

Fig. B.2 Variation of the experimental (Exp) and simulated (Sim) increase in Ca concentration (a) and output pH (b) with time in limestone column experiments at 25 °C (in green; *L25-atm-a3.5*) and 60 °C (in red; *L60-atm-a3.5*). Solid line in (b) shows input pH. Dashed and dotted lines show simulated values at 25 and 60 °C, respectively. 141

Fig. B.3 Variation of the experimental (Exp) and simulated (Sim) increase in Ca (a) and output pH (b) with time in limestone column experiments at 25 °C (in green; *L25-10-gp-u*) and 40 °C (in orange; *L40-10-gp-u*). Colored solid lines in (a) represent the Ca equilibrium with calcite and black-dashed line in (b) indicates input pH. Dashed and dotted lines show simulated values at 25 and 40 °C, respectively. 141

Fig. B.4 Experimental variation of volume of dissolved limestone V_{L-diss} (a) and porosity (b) versus time in experiments performed at 25 °C (in green; *L25-10-gp-u* and *L25-10-gp-e*), 40 °C (in orange; *L40-10-gp-u* and *L40-10-gp-e*) and 60 °C (in red; *L60-10-gp-e*). Solid and dashed lines indicate experiments with gypsum-equilibrated and gypsum-undersaturated solutions, respectively..... 142

List of tables

Table 1.1 Average composition of the Hontomín groundwater ($\pm 10\%$) in terms of total concentration (mol/kgw) and pH. It was provided by CIUDEN after extraction from the H-2 well.....	8
Table 2.1 Rock samples: origin and mineralogical composition (wt.%). See also Fig. 1.2....	14
Table 2.2 Injected solutions: amount of reagents, experimental conditions, average concentration (from ICP-AES), experimental pH, and calculated saturation indexes (SI), pH and ionic strength (I).....	19
Table 2.3 Reactive surface area (A_m) and input boundary conditions (SI, I and pH) used in simulations under atmospheric conditions (CrunchFlow code).....	31
Table 2.4 Reactive surface area (A_m) and input boundary conditions (SI, I and pH) used in simulations under subcritical and supercritical conditions (CrunchFlow and PhreeqC (v.3) codes).....	32
Table 2.5 Initial mineralogical composition of both the rock matrix and the high-permeability zone (fracture) and input solution used in the 2D simulations.	36
Table 2.6 Initial transport properties assumed in the 2D calculations.	37
Table 3.1 Experimental conditions and results (pH, volume of dissolved rock and precipitated mineral, porosity variation, and measured and calculated loss of mass) of the column experiments.	43
Table 4.1 List of the percolation experiments.....	62

Table 4.2 Measured (weighted) mass of fractured core (M_{meas}), fracture permeability (k), and fracture geometry (a and V) obtained by hydraulic measurement (a_h and V_h), XCMT (a_{Xr} and V_{Xr}) and SEM (a_s and V_s) at initial time ($t = t_0$).63

Table 4.3 Measured mass, measured and calculated loss of mass and variation in fracture volume determined from aqueous chemistry and XCMT at the end of the experimental runs ($t = t_f$).81

Table 4.4 Péclet (Pe) and Damköhler (Da) numbers and net reaction rates expressed as volume of dissolved calcite, precipitated gypsum and variation in fracture volume per time and injected volume.85

Table A.1 Experimental and input boundary conditions, transport parameters, numerical discretization and rock composition used in simulations of column experiments under atmospheric CO_2 conditions.130

Table A.2 Experimental and input boundary conditions, transport parameters, numerical discretization and rock composition used in simulations of column experiments under subcritical and supercritical CO_2 conditions.131

Table A.3 Equilibrium constants ($\log K$) and stoichiometric coefficients for equilibria in solution (column experiments and fractured core experiments *L0.2-gp-e* and *L1-gp-e*). Reactions are written as the destruction of 1 mol of the species in the first column. * indicates species used in the atmospheric CO_2 experiments with H_2SO_4 input solution (*s*).132

Table A.4 Equilibrium constants ($\log K$) and stoichiometric coefficients for mineral reactions (column experiments). Reactions are written as the dissolution of 1 mol of mineral.133

Table A.5 Parameters for the mineral reaction rate laws (column experiments). All parameters are from Palandri and Kharaka (2004), except for the coefficients m_1 and m_2 for calcite, which are based on the data reported by Xu et al. (2012).133

Table A.6 Experimental and input boundary conditions, fracture dimensions, numerical discretization, transport parameters and rock and fracture composition used in simulations of fractured core experiments.135

Table A.7 Equilibrium constants (log K) and stoichiometric coefficients for equilibria in solution in fractured core experiment *S60-no-s*. Reactions are written as the destruction of 1 mol of the species in the first column 136

Table A.8 Equilibrium constants (log K) and stoichiometric coefficients for mineral reactions (fractured core experiments). Reactions are written as the dissolution of 1 mol of mineral. 137

Table A.9 Parameters for the mineral reaction rate laws (fractured core experiments). Parameters for calcite, gypsum and quartz are from Palandri and Kharaka (2004), except for the coefficients m_1 and m_2 for calcite, which are based on the data reported by Xu et al. (2012). Parameters for microcline are from Bandstra et al. (2008). 137

